



Dual-mode thermal-regulating and self-powered pressure sensing hybrid smart fibers

Chuan Ning^{a,b,1}, Kai Dong^{a,b,1}, Wenchao Gao^{c,1}, Feifan Sheng^{a,d}, Renwei Cheng^{a,b}, Yang Jiang^{a,b}, Jia Yi^{a,d}, Cuiying Ye^{a,b}, Xiao Peng^{a,b}, Zhong Lin Wang^{a,b,e,*}

^a CAS Center for Excellence in Nanoscience, Beijing Key Laboratory of Micro-Nano Energy and Sensor, Beijing Institute of Nanoenergy and Nanosystems, Chinese Academy of Sciences, Beijing 100083, China

^b School of Nanoscience and Technology, University of Chinese Academy of Sciences, Beijing 100049, China

^c Department of Civil Engineering, Monash University 3800 Clayton, Australia

^d Center on Nanoenergy Research, School of Physical Science and Technology, Guangxi University, Nanning 530004, China

^e School of Material Science and Engineering, Georgia Institute of Technology, Atlanta, GA 30332, United States

ARTICLE INFO

Keywords:

Thermal-regulating
Triboelectric nanogenerators
Phase change
Self-powered
Pressure sensors
Multifunction fibers

ABSTRACT

Textiles are considered as the second skin of human beings, and one of its essential tasks is thermal management. Nowadays, textile-based wearable pressure sensing technology represents a fascinating developing trend due to its predominant breathability, moisture permeability, and excellent comfortability. At the same time, thermal-regulating textiles have also received extensive attention in academia and industrial fields, because they can provide personal thermal comfort for the human body. However, there are few textiles that have the dual functions of pressure sensing and thermal regulation. Herein, a novel and multifunctional smart fiber is fabricated by using a hollow silicone rubber fiber filled with a liquid metal (LM) electrode. It can automatically switch between heating mode and cooling mode to adjust microenvironment temperature around human skin through solid-liquid phase transformation of phase change materials (PCMs). In addition, as a self-powered pressure sensor, the fiber can respond to versatile mechanical stimuli, such as human walking, running, wrist movements, and joint bending at different angles. This work provides a feasible way for constructing multifunctional smart fibers, which show great application prospects in personal motion monitoring and real-time thermal regulation.

1. Introduction

Textiles are the basic necessities of human life, which are considered to be the second skin. Owing to their unique features and excellent performance, they have been widely used by humans for thousands of years. With the development of modern technology, textiles have been endowed with new missions of personal healthcare monitoring, motion sensing, and human-interfacing [1–3]. They are gradually developing towards information, network, and intelligence [4–6]. To this end, textile-based wearable pressure sensors have received considerable attentions [3,7–9]. In addition, it is also very important to maintain personal thermal comfort more effectively, which attracts widespread interests and contributes to the next generation of smart textiles.

Heating and air conditioning refrigeration of a building can provide

people with personal thermal comfort, but it consumes a large amount of energy, which accounts for a predominant part of energy consumption in our daily life [10–12]. Therefore, thermal regulation of the micro-environment around the human skin is considered as one of the most efficient ways. Research has shown that controlling the infrared optical properties of textiles can affect the localized temperature of human body [13–16]. However, due to the opposite requirements for optical properties, one type of textile can perform a single function of heating or cooling [11,17–21]. Liquid-solid phase transitions can be an attractive route for building a dual-mode thermal regulating system due to the wide range of phase transition temperatures. In addition, the whole process of storage and release thermal energy is reversible and does not require extra energy sources [22,23].

Triboelectric nanogenerators (TEGs), based on contact

* Corresponding author at: CAS Center for Excellence in Nanoscience, Beijing Key Laboratory of Micro-Nano Energy and Sensor, Beijing Institute of Nanoenergy and Nanosystems, Chinese Academy of Sciences, Beijing 100083, China.

E-mail address: zhong.wang@mse.gatech.edu (Z.L. Wang).

¹ These authors contributed equally to this work.

<https://doi.org/10.1016/j.cej.2021.129650>

Received 6 February 2021; Received in revised form 24 March 2021; Accepted 31 March 2021

Available online 7 April 2021

1385-8947/© 2021 Elsevier B.V. All rights reserved.

electrification and electrostatic induction [24–29], has been demonstrated to effectively convert mechanical stimulus into electrical signals [30–35]. In recent years, various types of wearable self-powered pressure sensors based on TENGs have been developed [36–40]. Among them, the textile-based TENGs present attractive prospects and unique advantages due to their versatile permeability and excellent comfortability [41–44]. In addition, this new class of wearable pressure sensors can conform to human organs while maintaining satisfactory reliability [45,46].

Herein, an innovative multifunction fiber is fabricated by filling the liquid metal (LM) into a hollow silicone rubber fiber. The LM acts as not only an electrode but also the phase change materials (PCMs) with a lower phase transformation point. The microencapsulated phase change materials (MPCMs) with a higher phase transformation point are dispersed throughout the silicone rubber. The dual-mode temperature regulating system can automatically switch between heating mode and cooling mode depending on the external environmental temperature. When the ambient temperature falls below 14 °C or exceeds over 28 °C, the fibers can release or absorb heat to provide a comfortable

microenvironment for the human body. At the same time, as self-powered tactile sensor, the fibers can respond to versatile mechanical stimuli, such as walking, wrist movements, and joints bending. It's worth noting that the silicone rubber fiber injected with LM is highly deformable and can be stretched without inducing elastic modulus mismatch. Therefore, the multifunction fiber can fully conform on human organs to monitor human motions.

2. Results and discussion

The methods of preparing the multifunction fibers are displayed in Fig. 1a and b. The fabrication steps consist of preparing silicone rubber solution, constructing hollow silicone rubber fiber (Fig. S1, Supporting Information), injecting LM, and adding conducting wires. The detailed process is described in the experimental section.

MPCMs are fabricated by encapsulating the PCMs inside of the microcapsules to form the shell-core structure. In this work, the paraffin as the core, melamine resin as the shell. As shown in Figs. 1c and S2 (Supporting Information), the MPCMs present a regular orbicular

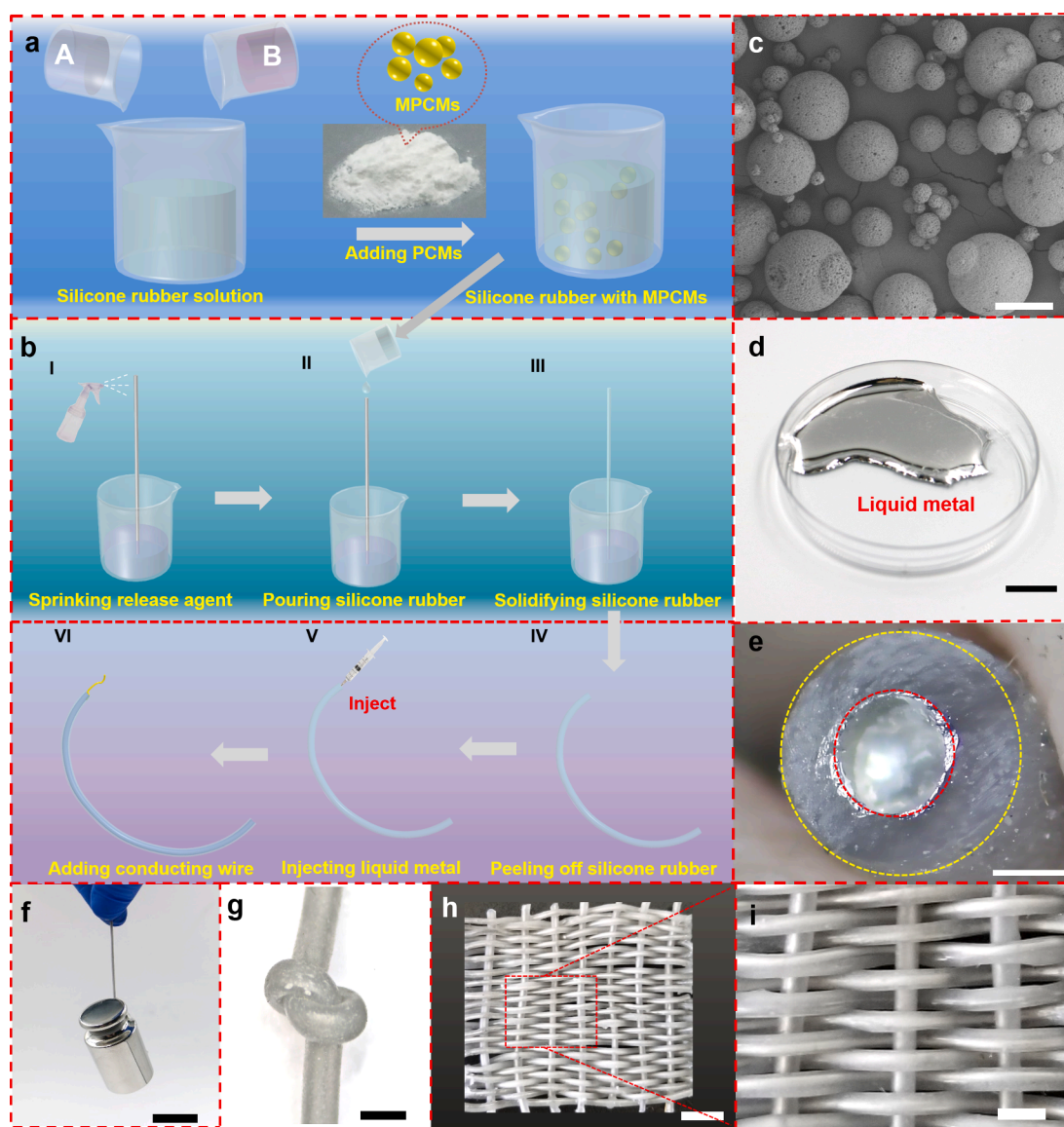


Fig. 1. Structure design, fabrication steps and mechanical properties of the multifunction fiber. a) The preparation of the silicone rubber solution. b) The fabrication steps of the multifunction fibers. c) SEM images of the MPCMs (scale bar: 50 μm). d) Photograph of the LM in a culture dish (scale bar: 1 cm). e) Cross-sectional micrograph of the multifunction fiber (scale bar: 500 μm). f) A single fiber that can withstand a weight of 100 g (scale bar: 2 cm). g) Photograph of the multifunction fiber knot (scale bar: 2 mm). (h) A textile base on the multifunction fibers (scale bar: 1 cm). (i) An enlarged photograph of the textile (scale bar: 3 mm).

structure, which makes them uniformly distributed in the silicone rubber. LM has received widespread attention due to its high conductivity, excellent fluidity, and negligible toxicity. Here, the metal (75.5% gallium and 24.5% indium) is selected as the electrode, which is liquid at room temperature (Fig. 1d). It can transform from liquid to solid and release heat in low-temperature environment. Silicone rubbers is a common material with a strong ability to acquire electrons, which acts as encapsulating material to form the external sheath. As displayed in Figs. 1e and S3 (Supporting Information), the cross-section of the multifunction fiber holds a clear core-sheath structure in which the outer layer and inner layer are silicone rubber and LM, respectively. And the diameters of the multifunction fibers are about 1.66 mm (Fig. S4, Supporting Information). In addition, the fibers have high strength and excellent flexibility. A single fiber can withstand a weight of 100 g, which can also sustain different mechanical deformations, including knotting, bending, and twisting, as exhibited in Figs. 1f, g and S5 (Supporting Information). The wearability tests are important for wearable device, a corresponding bending test on the fiber is performed. As shown in Fig. S6 (Supporting Information), there is no significant change in the V_{OC} of the fiber after 10,000 times of bending, which reveals that the fiber possesses a good wearability. In order to test the washability of the fibers, the fibers are agitated in a beaker with water by a magnetic stirrer for laundering of 30 min. Fig. S7 (Supporting

Information) shows the V_{OC} of the unwashed and after repeated washing cycles. It can be clearly seen that with the number of washing times increased, the fiber can still generates electricity steadily and the peak V_{OC} slightly declined. The multifunction fibers can be further woven into a textile with a plain weave structure (Fig. 1h and i). All of the above show that the multifunction fibers possess the potential application prospects in the field of wearable technology.

Fig. 2a is the schematic diagram of the multifunction fibers. It can be clearly seen that the fibers consist of two kinds of phase change materials: LM and MPCMs. LM is the core of fiber, and the MPCMs disperse throughout the silicone rubber. The multifunction fibers can realize the dual functions of both heating and cooling through the PCMs with different phase transformation points to work cooperatively, Fig. 2b shows the working mechanism of temperature regulation. When the ambient temperature falls below the phase transformation point of LM, the LM changes from liquid to solid, in which heat is released (heating mode). The MPCMs change from solid to liquid with heat absorption while the outside temperature exceeds the phase transformation point of MPCMs (cooling mode).

The electricity-generation mechanism of the fibers follows the single-electrode mode. The potential distribution in three different states is simulated by the COMSOL software (Fig. 2c), and the electrical potential difference is capable of driving free electrons to flow between the

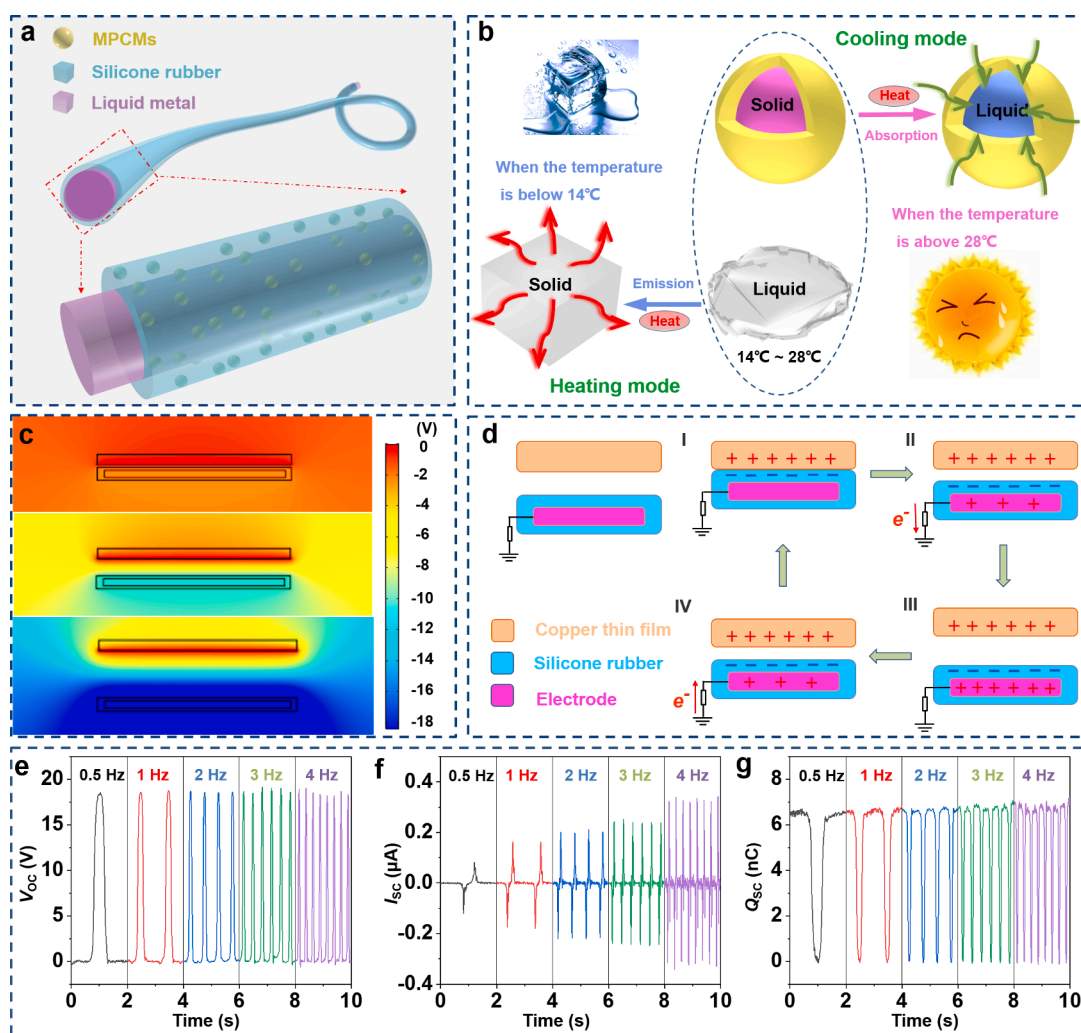


Fig. 2. Mechanism of thermal regulation and electricity-generation and the electrical outputs of the multifunction fibers at different frequencies. a) Schematic structure diagram of the multifunction fiber. b) Thermal-regulating mechanism diagram of the multifunction fibers. c) Simulated electrical potential distribution in different working state of the multifunction fiber by the COMSOL software. d) Schematic of the electrons transfer process. e) V_{OC} , f) I_{sc} , and g) Q_{sc} of the multifunction fiber at different frequencies (0.5–4 Hz).

electrode and ground. The detailed principle is schematically shown in Fig. 2d. The silicone rubber (shell) and the LM (core) serve as triboelectric material and conductive electrodes, respectively. In the initial state, the copper thin film contacts with silicone rubber. Owing to the different electron trapping capability, electrons transfer from copper thin film to silicone rubber, generating the same number of positive charges and negative charges on the copper thin film and silicone rubber, respectively (step i). Once the copper thin film is separated from the silicone rubber surface, the electric potential of the electrode rises, which drives free electrons from the electrode through external loading to the ground (step ii). Afterward, the copper thin film continues to move away from the silicone rubber, until an equal number of inductive charges is generated on the electrode, achieving an electrostatic equilibrium (step iii). Conversely, when the copper thin film approaches the silicone rubber, the electrons flow from the ground to the electrode to neutralize the positive charge, producing a reversed current (step iv). This is a contact-separation cycle, continuous contact-separation movements bring continuous alternating current outputs.

A multifunction fiber with length of 5 cm is used for the electrical output performance test. A piece of Cu film is driven by a linear motor, it periodically contacts with the multifunction fiber when the linear motor works. Firstly, the outputs of the multifunction fibers are tested under different frequencies ranging from 0.5 to 4 Hz. On the one hand, the short-circuit current (I_{SC}) increases from 0.08 to 0.33 μA as the frequencies increase (Fig. 2f), revealing a clearly enhanced trend. This is ascribed to that the current is defined as the number of charges passing through cross-section of a conductor in unit time, which is positively correlated with working frequency [47]. On the other hand, the open-circuit voltage (V_{OC}) and short-circuit charge transfer (Q_{SC}) remain almost constant at ~ 18.5 V and ~ 6.8 nC, respectively (Fig. 2e, g). The inconsistent variation of electrical outputs with different loading frequency is explained in Fig. S8 (Supporting Information). The output power is calculated by $W = I^2R$, where I is the output current and R is the load resistance. As shown in Fig. 3a, the output power density increases with the increment of the applied external resistances. It can reach a peak value of $192 \mu\text{W m}^{-1}$ when the external load resistance is about 1.5

G Ω . The stability of the multifunction fibers is tested under 1 Hz for 5 h. It can be seen from Fig. 3b that the multifunction fibers can continue to work steadily. The V_{OC} has no attenuation and stably sustains around 18.6 V, the insets are the detailed V_{OC} curves during the early 10 cycles and the last 10 cycles. In order to further test the durability of the fiber the stability testing is repeated 10 times, and each measurement time is 5 h. As exhibited in Fig. S9 (Supporting Information), the fiber can still generate electricity steadily after 50 h of operation. The contact force is a key factor affecting the electric outputs of the multifunction fibers. As shown in Fig. 3c, a linear relationship is presented between the electric outputs and contact force, demonstrating that the larger contact force brings about a higher electric output, thereby endowing the fiber with an excellent capability to sense different loads. The results can be attributed to that the increased contact force enlarges contact area resulting in more triboelectric charges (Fig. S10, Supporting Information).

Stretchability is a significant property of fibers. The multifunction fibers have excellent stretchability because they are composed of stretchable silicon rubber injected with LM, which can be stretched without inducing elastic modulus mismatch., It can be seen from the stress-strain curve (Fig. 3g) that the multifunction fiber can be stretched to about 400%. Fig. S11 (Supporting Information) and the insets of Fig. 3g show the photos of the multifunction fibers being stretched. The electrical outputs are further measured when the multifunction fiber is stretched from 20% to 400%. As shown in Fig. 3d–f, the electrical outputs initially increase and then decrease with the increase of the stretching. The maximal V_{OC} , I_{SC} , and Q_{SC} reach 25.8 V, 0.17 μA and 8.3 nC, respectively. The reason may be that the fiber diameter decreases slightly with the increase of tensile strain at the beginning, but the friction layer becomes thinner, which leads to a higher electrostatic induction effect. Then the diameter of the fiber decreases significantly with the increase of the tensile amount, resulting in a smaller contact area. In addition, due to the reduction of the cross-sectional area of LM, the resistance of the multifunction fibers increases with the increment of tensile strains. As illustrated in Fig. 3h, when it is stretched to 400%, the resistance of the multifunction fiber increases from 0.4 Ω to 3.8 Ω , which

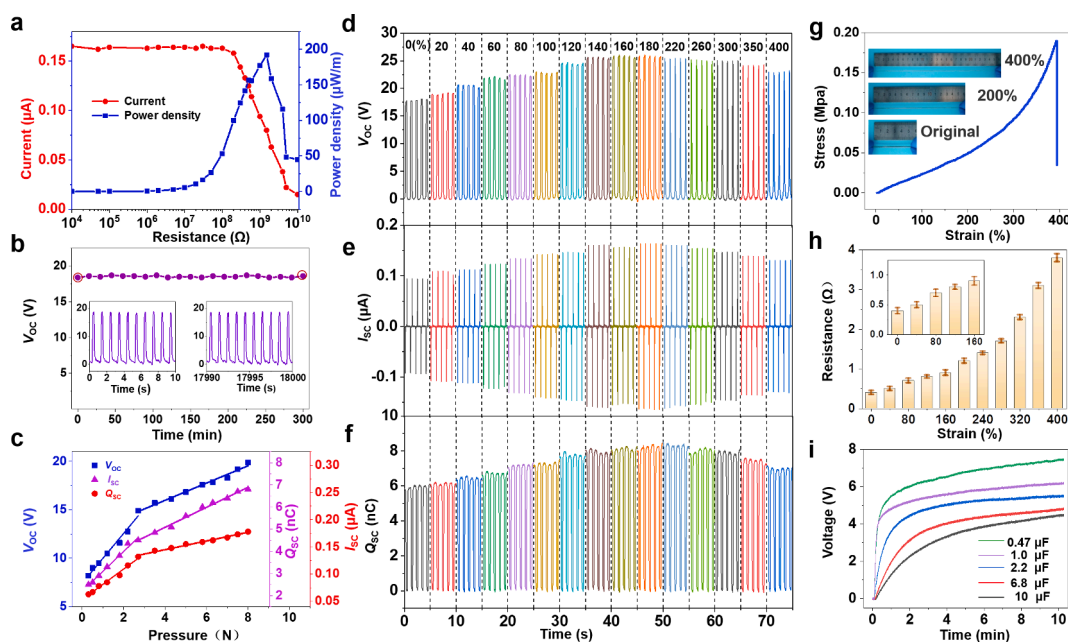


Fig. 3. The electrical outputs of the multifunction fiber under different conditions. a) Current and power density of the multifunction fiber at the different external loading resistance with a fixed frequency of 1 Hz. b) The stability of the multifunction fiber is tested under 1 Hz frequency for 5 h. c) Dependence of the V_{OC} , I_{SC} and Q_{SC} on the pressure. d) V_{OC} , e) I_{SC} , and f) Q_{SC} of the multifunction fiber at different tensile strain levels (0–400%). g) The strain-tension of the multifunction fiber, insets show the multifunction fiber being stretched. h) The electric resistance of a 5 cm multifunction fiber at different tensile strain levels (0–400%). i) Charging curve of the multifunction fiber with different capacitance.

has little negative impacts on the electrical outputs. Moreover, in order to explore the effects of diameter on electrical output, the multifunction fibers with different diameters are designed (Fig. S12, Supporting Information). It can be seen from Fig. S13 (Supporting Information) that the electrical outputs initially increase and then decrease as the diameter of the multifunction fibers increase. The reasons can be ascribed to a larger diameter means a larger contact area, but excessive increase in diameter result in a lower electrostatic induction effect. In addition, the multifunction fibers have the potential to store electricity in commercial capacitors and serve as a direct-current power supply. As displayed in Fig. 3i, the alternating current (AC) output generated by the multifunction fibers is converted to direct current (DC) output through a bridge circuit then used to charge the different capacitance capacitors (0.47 μF , 1 μF , 2.2 μF , 6.8 μF , 10 μF). It can be clearly seen that all the capacitors can reach above 3 V within 4 min (The length of the fiber is 5 cm and the contact frequency is 1 Hz).

The thermal-regulating performance of the PCMs is demonstrated by measuring the temperatures of a pair of identical test tubes in a high and low-temperature test chamber. As shown in Fig. S14 (Supporting Information), an empty test tube as the blank group and the other contains PCMs as the experimental group. The test chamber with controllable temperature can be used to effectively simulate the temperature of the natural environment. The curves are produced by simultaneously measuring the temperatures of the two groups. Fig. 4a exhibits the temperature-time curves of the blank group and experimental group (a test tube contains MPCMs). Initially, the temperatures of the two groups increase as the temperature of the test chamber rises. Once the temperature reaches the phase transition point of the MPCMs, the MPCMs

start to melt and absorb the thermal energy around them. It is observed that the temperature in the experimental group stays around 30 °C for a long time while that of blank group keeps rising (Fig. S15a, Supporting Information). The temperature in the experimental group is slightly higher than that of the phase transition point of MPCMs, the result may be related to the continuous increase in the temperature of the test chamber. Then, the temperature in the blank group drops with the environment temperature decline, whereas there is a corresponding heat release process in the experimental group (Fig. S15b, Supporting Information). As shown in Fig. 4b and e, the temperature change curves of the blank group are set as $Y = X$ (blue lines), which are used as the reference line to compare with the temperatures of the experimental group. It can be seen from Fig. 4b that the MPCMs have an obvious effect on thermal regulation. Moreover, the heat-storage capacity of the MPCMs is evaluated by the differential scanning calorimeter (DSC). In the solid-liquid transition, the phase transition temperature and melting enthalpies of MPCMs are 28.09 °C and 97.01 J g⁻¹, respectively (Fig. 4c).

The metal is liquid at room temperature, when the temperature drops to the phase transition point of the metal, it changes from liquid to solid and releases heat. Fig. 4d presents the temperature-time curves of the blank group and experimental group (a test tubes contains LM). The temperature of the experimental group is higher than the blank group when the temperature of the test chamber drops continuously. As shown in Figs. 4e and S16 (Supporting Information), the temperatures of the two groups show the same trend, while the experimental group have a heat storage and release process. The DSC curve of the LM is illustrated in Fig. 4f, the solidification temperature and solidification latent heat of

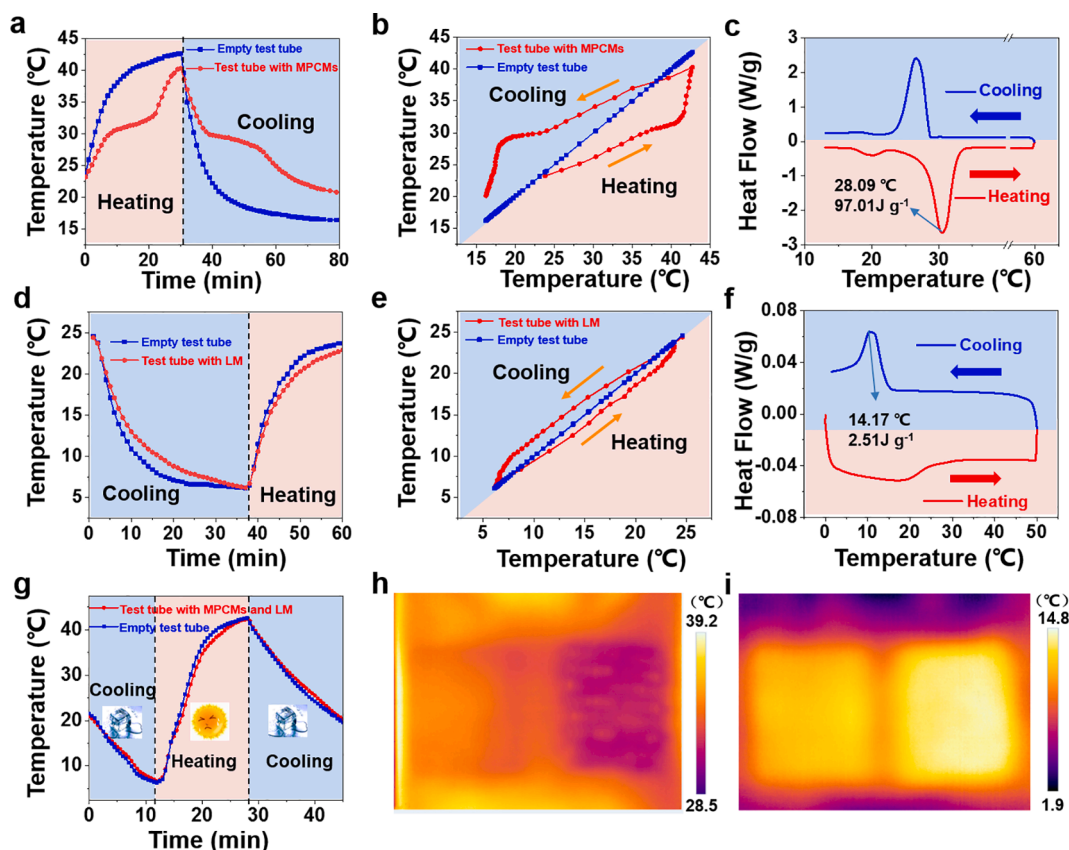


Fig. 4. The thermal-regulating performance of the PCMs. a) Temperature-time curves of the blank group and experimental group. The experimental group is a test tube contains MPCMs. b) Temperature change of the blank group is set as $Y = X$ (blue lines), comparing with the temperatures of the experimental group (a test tube contains MPCMs). c) DSC measurements of MPCMs. d) The temperature-time curves of the blank group and experimental group, the experimental group is a test tube contains LM. e) Temperature change of the blank group is set as $Y = X$, comparing with the temperatures of the experimental group (a test tube contains LM). f) DSC measurements of LM. g) Temperature-time curves of the blank group and experimental group, the experimental group is a test tube contains MPCMs and LM. Infrared images of common textile and multifunction fiber-based textile in a h) high temperature environments and i) low temperature environments.

LM are $14.17\text{ }^{\circ}\text{C}$ and 2.51 J g^{-1} , respectively. Therefore, the LM can give off some heat and effectively alleviate the temperature drop. In addition, the MPCMs and the LM are put into a test tube as the experimental group. As displayed in Fig. 4g, the MPCMs and the LM can work collectively, when the temperature is too high, MPCMs liquefy and absorb heat. Correspondingly, the LM solidifies and releases heat when the temperature is too low, Fig. S17 (Supporting Information) displays the details of temperature change. Moreover, the temperature change of the blank group is set as $Y = X$, comparing with the temperature change of experimental group (a test tube contains MPCMs and LM). As exhibited in Fig. S18 (Supporting Information), during the process of temperature rise, the temperature first reaches the phase change point of LM, where the LM liquefy and absorb heat, then the temperature reaches the phase change point of PCMs, where the PCMs liquefy and absorb heat. On the contrary, during the process of temperature drop the two kinds of PCMs solidify and give off heat. All of the results consistently suggest that the PCMs can effectively regulate temperature, verifying it can be applied to the dual-mode thermal-regulating systems.

The thermal-regulating property of the textile based on the multi-function fibers is demonstrated by comparing the real-time temperatures of the textile with a common textile in high and low temperature environments, respectively. An infrared camera is used to measure the real-time temperatures of the textiles. In order to verify that the samples are fully touched with the heating or cooling sources, two kinds of textiles are covered and tightened with a common cloth, as exhibited in Fig. S19 (Supporting Information). Firstly, the two textiles are compared by placing them on a heating plate. As illustrated in Movie 1 (Supporting Information), the temperatures of the two textiles are consistent at the beginning. As the heating plate temperature rises, the temperature of the textile based on the multifunction fibers is lower than cotton textile because the MPCMs absorb heat (Fig. 4h). Then both of them are placed in a low temperature environment. As displayed in Movie 2 (Supporting Information), because LM gives off heat during the phase transitions, the temperature of the textile based on the multifunction fibers is higher than cotton textile (Fig. 4i). All of these further confirms the textile based on the multifunction fibers can regulate the temperature

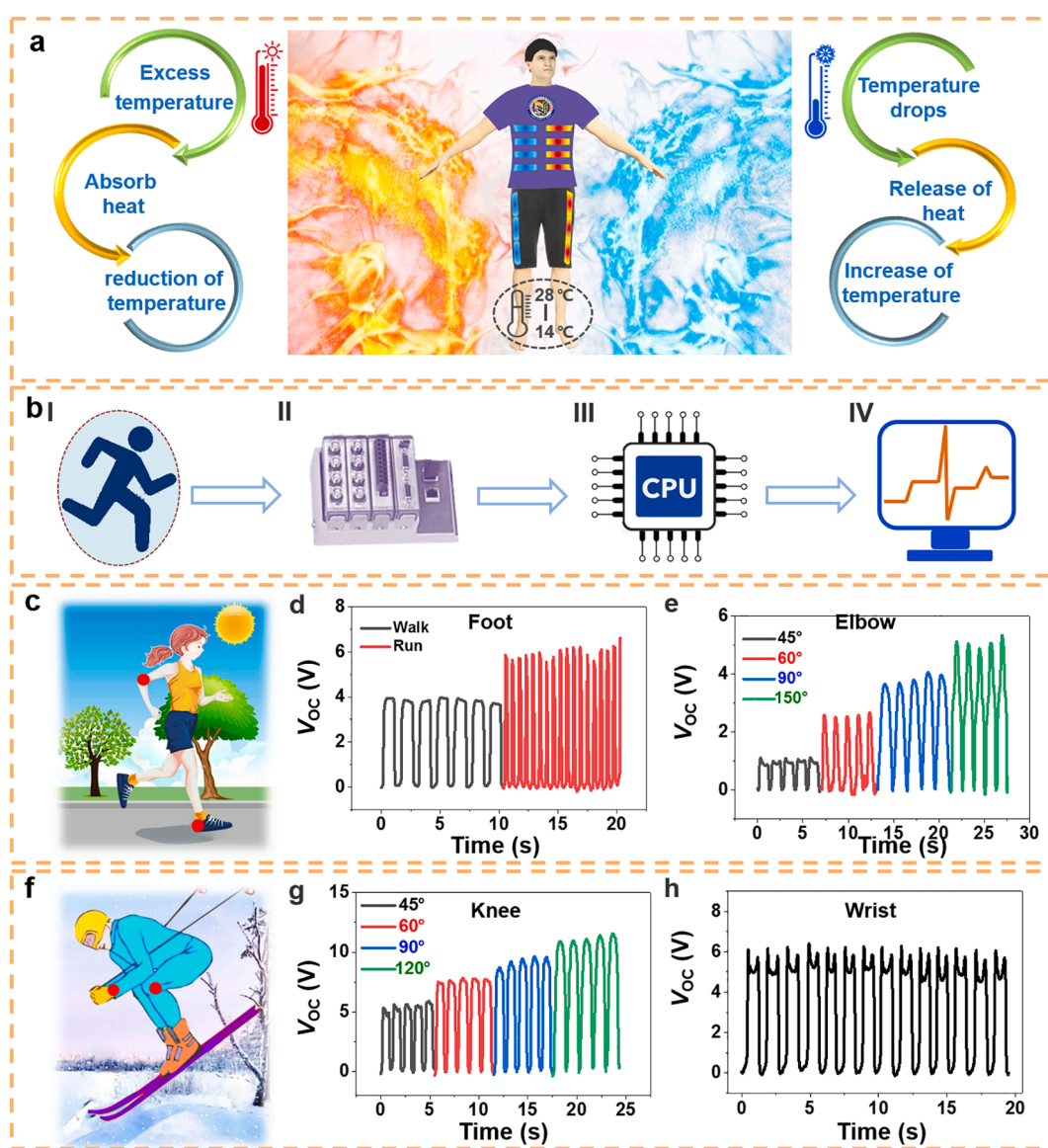


Fig. 5. Application of thermal regulation and motion monitoring. a) Mechanism of thermal regulation b) Sensing mechanism of the human motion monitoring system. The two application scenarios: c) a person is running on a hot summer day and f) a man is skiing in the snow. d) V_{OC} of a multifunction fiber attached on the heel when the personal is walking and running. e and g) V_{OC} of the multifunction fibers that are fixed at the elbow and knee joints, respectively, when the joints bend different angles. h) V_{OC} of the multifunction fiber for monitoring wrist motion states.

effectively.

Thermal regulation through wearable technology has attracted increasing attention, due to it can provide personal thermal comfort in a low-cost and energy-saving way. The textiles have an effect on localized temperature of the human body by controlling the infrared optical properties. But one type of textile can perform a single function of heating or cooling [48], which cannot adapt to the changes of ambient temperature. Here, we demonstrate a kind of fiber based on the PCMs with different phase transformation points. As shown in the schematic illustration (Fig. 5a), when the human is exposed to an environment below 14 °C, the LM begins to solidify and release heat, raising the temperature of the microenvironment around the body. On the contrary, when the human body in an environment higher than 28 °C, the MCPMs begin to liquefy and absorb heat, cooling the microenvironment near the human skin. The whole process of thermal regulation is reversible and does not require extra energy sources. In addition, it can achieve thermal energy storage and release with the variation of temperature. This shows that multifunction fibers can provide the human body thermal comfort in hot and cold environments.

The multifunction fibers can not only regulate temperature but also act as self-powered pressure sensors. The sensing mechanism is shown in Fig. 5b, a self-powered human motion monitoring system consists of signal acquisition module and signal processing module. As the multifunction fibers are triggered and generates electrical signals, the data is collected and processed by a data acquisition card and a specialized developed data processing software, respectively. Based on their excellent pressure sensitivity, thermal-regulating ability, and high flexibility, the multifunction fibers can be integrated into specific parts of human body, such as the feet, knees, and elbows to regulate the temperatures and recognize the motion signals. Two familiar application scenarios are shown in Fig. 5c and f. Fig. 5c depicts a person that is running on a hot summer day. In this scenario, the multifunction fibers can not only effective against high external temperature, but also record the number of steps, stride frequency and arm-swinging posture. As exhibited in Fig. 5f, a man is skiing in the snow. At this point, the multifunction fibers can provide heat for the person and meanwhile monitor his movements when skiing. As exhibited in Fig. 5d, there are obvious differences in the frequency and amplitude, we can easily distinguish walking from running and calculate the number of steps and stride frequency by these electrical signals. In addition, the multifunction fibers can also recognize joint motions at different bending angles, such as the knees, elbows, and fingers. For example, the fibers are fixed to the elbow and knee to monitor their bending angles. The relationship between the bending angles and the V_{OC} as shown in Fig. 5e and g, different bending angles correspond to different V_{OC} , and the V_{OC} increases with the increase of bending angles. This is because as the increase of bending angles of the joints, the contact area and contact force increase between the skin and the fibers and the silicone rubber on the outer layer of the fiber becomes thin, all of these changes enhance electrostatic induction. By the same principle, the multifunction fibers can also monitor the bending angle of the fingers, as illustrated in Fig. S20 (Supporting Information). The wrist movements can also be monitored by fixing the fibers to the wrist (Fig. 5h). The driving force for skiing comes from the ski poles when a person is skiing, and the usage of ski poles can be effectively obtained by monitoring the movements of fingers, wrists and elbows. Therefore, the multifunction fibers have potential applications for learner to master the skills of using ski poles.

3. Conclusion

In summary, a multifunctional smart fiber is developed by injecting liquid metal into a hollow silicone rubber tube. The fiber contains two kinds of PCMs, which can regulate the temperature of the microenvironment around the human skin and provide personal thermal comfort. Moreover, the fiber can act as a self-powered pressure sensor to respond to mechanical stimuli. A fiber with the length of 5 cm can generate a V_{OC}

of 18.5 V, the instantaneous electric power density can reach a peak value of $192 \mu\text{W m}^{-1}$. Based on the excellent electrical output performance, the multifunction fiber can generate electrical signals while it is triggered by the human body. These electrical signals from different parts of the body can be used to monitor different human movements. The work provides a valuable reference for the study of multi-responsive smart fibers.

4. Experimental section

4.1. Materials

The scalable and non-toxic silicone rubber was chosen as the frictional layer material. The metal is liquid at room temperature and it is both electrode and PCMs with a lower phase transition point. The LM was injected into a hollow silicone rubber fiber to form multifunction fiber. MPCMs contain PCMs with higher phase change points, which dispersed throughout the silicone rubber.

4.2. Preparation of silicone rubber solution

The silicone rubber solution is divided into liquid A and liquid B. Mixed the two components of the liquid silicone rubber in a 1:1 wt ratio. Then added MPCMs and mixed well to make a silicone rubber mixed solution.

4.3. Fabrication of hollow silicone rubber fiber

Firstly, release agent was sprinkled over a copper wire (I) then the prepared mixed solution was poured over the copper wire with a diameter of 0.8 mm and evenly spread to the copper wire surface under the action of gravity (II). Finally, after solidifying at room temperature (III), a hollow silicone rubber fiber was peeled off from the copper wire (IV).

4.4. Fabrication of the multifunction fibers

Firstly, the LM was injected slowly with a syringe from one end of the hollow silicone rubber fiber until the LM filled the entire fiber (V). Secondly, a wire was inserted into the silicone rubber fiber and came into contact with the LM. Finally, the two ends of the fiber were sealed with silicone rubber solution (VI).

4.5. Characterization and measurement

A Hitachi SU8020 field emission SEM was employed to observe the morphology of MPCM and the section of hollow silicone rubber fiber. An electron microscope was used for enlarged core-sheath structure of the multifunction fibers. The electrical outputs of the multifunction fibers were measured by a Keithley 6514 electrometer. Infrared camera (GMATG-A4) was used to measure the temperatures of the textiles. Differential scanning calorimeter (TA, Q20) was used to measure the DSC curve of PCMs.

Declaration of Competing Interest

The authors declare that they have no known competing financial interests or personal relationships that could have appeared to influence the work reported in this paper.

Acknowledgments

The authors are grateful for the support received from the National Key R & D Project from Minister of Science and Technology (Grant No. 2016YFA0202704), the Beijing Municipal Natural Science Foundation (Grant No. 2212052), the Shanghai Sailing Program (Grant No.

19S28101) and the Fundamental Research Funds for the Central Universities (Grant No. 19D128102). Informed consent was obtained from the volunteers who participated in the experiments.

Appendix A. Supplementary data

Supplementary data to this article can be found online at <https://doi.org/10.1016/j.cej.2021.129650>.

References

- [1] K. Dong, X. Peng, J. An, A.C. Wang, J. Luo, B. Sun, J. Wang, Z.L. Wang, Shape adaptable and highly resilient 3D braided triboelectric nanogenerators as e-textiles for power and sensing, *Nat. Commun.* 11 (1) (2020) 2868.
- [2] Wenjing Fan, Qiang He, Keyu Meng, Xulong Tan, Zhihao Zhou, Gaoqiang Zhang, Jin Yang, Z.L. Wang, Machine-knitted washable sensor array textile for precise epidermal physiological signal monitoring, *Sci. Adv.* 6 (2020).
- [3] A. Leber, C. Dong, R. Chandran, T. Das Gupta, N. Bartolomei, F. Sorin, Soft and stretchable liquid metal transmission lines as distributed probes of multimodal deformations, *Nat. Electron.* 3 (6) (2020) 316–326.
- [4] L. Wang, L. Wang, Y. Zhang, J. Pan, S. Li, X. Sun, B. Zhang, H. Peng, Weaving sensing fibers into electrochemical fabric for real-time health monitoring, *Adv. Funct. Mater.* 28 (42) (2018) 1804456.
- [5] C. Zhu, R. Li, X. Chen, E. Chalmers, X. Liu, Y. Wang, B.B. Xu, X. Liu, Ultraelastic yarns from curcumin-assisted ELD toward wearable human-machine interface textiles, *Adv. Sci.* 7 (23) (2020) 2002009.
- [6] K. Dong, X. Peng, Z.L. Wang, Fiber/fabric-based piezoelectric and triboelectric nanogenerators for flexible/stretchable and wearable electronics and artificial intelligence, *Adv. Mater.* (2019), e1902549.
- [7] F. Wen, Z. Sun, T. He, Q. Shi, M. Zhu, Z. Zhang, L. Li, T. Zhang, C. Lee, Machine learning glove using self-powered conductive superhydrophobic triboelectric textile for gesture recognition in VR/AR applications, *Adv. Sci.* 7 (14) (2020) 2000261.
- [8] Y. Zhang, M. Tian, L. Wang, H. Zhao, L. Qu, Flexible Janus textile-based electroosmotic pump for large-area unidirectional positive water transport, *Adv. Mater. Interfaces* 7 (13) (2020) 1902133.
- [9] C. Ning, K. Dong, R. Cheng, J. Yi, C. Ye, X. Peng, F. Sheng, Y. Jiang, Z.L. Wang, Flexible and stretchable fiber-shaped triboelectric nanogenerators for biomechanical monitoring and human-interactive sensing, *Adv. Funct. Mater.* 2006679 (2020).
- [10] S. Chu, A. Majumdar, Opportunities and challenges for a sustainable energy future, *Nature* 488 (7411) (2012) 294–303.
- [11] Po-Chun Hsu, Chong Liu, Alex Y. Song, Ze Zhang, Yucan Peng, Jin Xie, Kai Liu, Chun-Lan Wu, Peter B. Catrysse, Lili Cai, Shang Zhai, Arun Majumdar, Shanhui Fan, Y. Cui, A dual-mode textile for human body radiative heating and cooling, *Sci. Adv.* 3 (2017) e1700895.
- [12] L. Pérez-Lombard, J. Ortiz, C. Pout, A review on buildings energy consumption information, *Energy Build.* 40 (3) (2008) 394–398.
- [13] A. Choe, J. Yeom, Y. Kwon, Y. Lee, Y.-E. Shin, J. Kim, H. Ko, Stimuli-responsive micro/nanoporous hairy skin for adaptive thermal insulation and infrared camouflage, *Mater. Horiz.* 7 (12) (2020) 3258–3265.
- [14] E.M. Leung, M. Colorado Escobar, G.T. Stubiannu, S.R. Jim, A.L. Vyatskikh, Z. Peng, N. Garner, P. Patel, K.L. Naughton, M. Follador, E. Karshalev, M.D. Trexler, A. A. Gorodetsky, A dynamic thermoregulatory material inspired by squid skin, *Nat. Commun.* 10 (1) (2019) 1947.
- [15] P.-C. Hsu, Alex Y. Song, Peter B. Catrysse, Chong Liu, Yucan Peng, J. Xie, Shanhui Fan, Y. Cui, Radiative human body cooling by nanoporous polyethylene textile, *Science* 353 (6303) (2016) 1019–1023.
- [16] P.C. Hsu, X. Liu, C. Liu, X. Xie, H.R. Lee, A.J. Welch, T. Zhao, Y. Cui, Personal thermal management by metallic nanowire-coated textile, *Nano Lett.* 15 (1) (2015) 365–371.
- [17] L. Cai, Y. Peng, J. Xu, C. Zhou, C. Zhou, P. Wu, D. Lin, S. Fan, Y. Cui, Temperature regulation in colored infrared-transparent polyethylene textiles, *Joule* 3 (6) (2019) 1478–1486.
- [18] Y. Cui, H. Gong, Y. Wang, D. Li, H. Bai, A thermally insulating textile inspired by polar bear hair, *Adv. Mater.* 30 (14) (2018), e1706807.
- [19] T. Gao, Z. Yang, C. Chen, Y. Li, K. Fu, J. Dai, E.M. Hitz, H. Xie, B. Liu, J. Song, B. Yang, L. Hu, Three-dimensional printed thermal regulation textiles, *ACS Nano* 11 (11) (2017) 11513–11520.
- [20] C. Tan, Z. Dong, Y. Li, H. Zhao, X. Huang, Z. Zhou, J.W. Jiang, Y.Z. Long, P. Jiang, T.Y. Zhang, B. Sun, A high performance wearable strain sensor with advanced thermal management for motion monitoring, *Nat. Commun.* 11 (1) (2020) 3530.
- [21] D. Li, X. Liu, W. Li, Z. Lin, B. Zhu, Z. Li, J. Li, B. Li, S. Fan, J. Xie, J. Zhu, Scalable and hierarchically designed polymer film as a selective thermal emitter for high-performance all-day radiative cooling, *Nat. Nanotechnol.* (2020).
- [22] D. Luo, L. Xiang, X. Sun, L. Xie, D. Zhou, S. Qin, Phase-change smart lines based on paraffin-expanded graphite/polypropylene hollow fiber membrane composite phase change materials for heat storage, *Energy* 197 (2020), 117252.
- [23] W. Xia, X. Fei, Q. Wang, Y. Lu, M.T. Innocent, J. Zhou, S. Yu, H. Xiang, M. Zhu, Nano-hybridized form-stable ester@F-SiO₂ phase change materials for melt-spun PA6 fibers engineered towards smart thermal management fabrics, *Chem. Eng. J.* 403 (2021), 126369.
- [24] Z.L. Wang, On Maxwell's displacement current for energy and sensors: the origin of nanogenerators, *Mater. Today* 20 (2) (2017) 74–82.
- [25] C. Xu, B. Zhang, A.C. Wang, H. Zou, G. Liu, W. Ding, C. Wu, M. Ma, P. Feng, Z. Lin, Z.L. Wang, Contact-electrification between two identical materials: curvature effect, *ACS Nano* 13 (2) (2019) 2034–2041.
- [26] W.T. Cao, H. Ouyang, W. Xin, S. Chao, C. Ma, Z. Li, F. Chen, M.G. Ma, A stretchable highoutput triboelectric nanogenerator improved by MXene liquid electrode with high electronegativity, *Adv. Funct. Mater.* 30 (50) (2020) 2004181.
- [27] L. Jin, W. Deng, Y. Su, Z. Xu, H. Meng, B. Wang, H. Zhang, B. Zhang, L. Zhang, X. Xiao, M. Zhu, W. Yang, Self-powered wireless smart sensor based on maglev porous nanogenerator for train monitoring system, *Nano Energy* 38 (2017) 185–192.
- [28] X. Qu, X. Ma, B. Shi, H. Li, L. Zheng, C. Wang, Z. Liu, Y. Fan, X. Chen, Z. Li, Z. L. Wang, Refreshable braille display system based on triboelectric nanogenerator and dielectric elastomer, *Adv. Funct. Mater.* 31 (5) (2020) 2006612.
- [29] Q. Zheng, Q. Tang, Z.L. Wang, Z. Li, Self-powered cardiovascular electronic devices and systems, *Nat. Rev. Cardiol.* 18 (1) (2021) 7–21.
- [30] F.R. Fan, L. Lin, G. Zhu, W. Wu, R. Zhang, Z.L. Wang, Transparent triboelectric nanogenerators and self-powered pressure sensors based on micropatterned plastic films, *Nano Lett.* 12 (6) (2012) 3109–3114.
- [31] X. Peng, K. Dong, C. Ye, Y. Jiang, S. Zhai, R. Cheng, D. Liu, Xiaoping Gao, J. Wang, Z.L. Wang, A breathable, biodegradable, antibacterial, and self-powered electronic skin based on all-nanofiber triboelectric nanogenerators, *Sci. Adv.* 6 (2020) eaba9624.
- [32] K. Dong, J. Deng, Y. Zi, Y.C. Wang, C. Xu, H. Zou, W. Ding, Y. Dai, B. Gu, B. Sun, Z. L. Wang, 3D orthogonal woven triboelectric nanogenerator for effective biomechanical energy harvesting and as self-powered active motion sensors, *Adv. Mater.* 29 (38) (2017).
- [33] K. Dong, Z. Wu, J. Deng, A.C. Wang, H. Zou, C. Chen, D. Hu, B. Gu, B. Sun, Z. L. Wang, A stretchable yarn embedded triboelectric nanogenerator as electronic skin for biomechanical energy harvesting and multifunctional pressure sensing, *Adv. Mater.* 30 (43) (2018), e1804944.
- [34] Y. Tang, H. Zhou, X. Sun, N. Diao, J. Wang, B. Zhang, C. Qin, E. Liang, Y. Mao, Triboelectric touch-free screen sensor for noncontact gesture recognizing, *Adv. Funct. Mater.* 30 (5) (2019) 1907893.
- [35] D. Jiang, B. Shi, H. Ouyang, Y. Fan, Z.L. Wang, Z. Li, Emerging implantable energy harvesters and self-powered implantable medical electronics, *ACS Nano* 14 (6) (2020) 6436–6448.
- [36] C. Chen, L. Chen, Z. Wu, H. Guo, W. Yu, Z. Du, Z.L. Wang, 3D double-faced interlock fabric triboelectric nanogenerator for bio-motion energy harvesting and as self-powered stretching and 3D tactile sensors, *Mater. Today* (2019).
- [37] R. Cao, X. Pu, X. Du, W. Yang, J. Wang, H. Guo, S. Zhao, Z. Yuan, C. Zhang, C. Li, Z. L. Wang, Screen-printed washable electronic textiles as self-powered touch/gesture tribo-sensors for intelligent human-machine interaction, *ACS Nano* 12 (6) (2018) 5190–5196.
- [38] Y. Jiang, K. Dong, X. Li, J. An, D. Wu, X. Peng, J. Yi, C. Ning, R. Cheng, P. Yu, Z. L. Wang, Stretchable, washable, and ultrathin triboelectric nanogenerators as skin-like highly sensitive self-powered haptic sensors, *Adv. Funct. Mater.* 2005584 (2020).
- [39] Z. Li, Q. Zheng, Z.L. Wang, Z. Li, Nanogenerator-based self-powered sensors for wearable and implantable electronics, *Research* 2020 (2020) 8710686.
- [40] P. Tan, Y. Zou, Y. Fan, Z. Li, Self-powered wearable electronics, *Wearable Technol.* (2020) 1.
- [41] C. Ning, L. Tian, X. Zhao, S. Xiang, Y. Tang, E. Liang, Y. Mao, Washable textile-structured single-electrode triboelectric nanogenerator for self-powered wearable electronics, *J. Mater. Chem. A* 6 (39) (2018) 19143–19150.
- [42] Z. Zhou, K. Chen, X. Li, S. Zhang, Y. Wu, Y. Zhou, K. Meng, C. Sun, Q. He, W. Fan, E. Fan, Z. Lin, X. Tan, W. Deng, J. Chen, Sign-to-speech translation using machine-learning-assisted stretchable sensor arrays, *Nat. Electron.* 3 (9) (2020) 571–578.
- [43] H.J. Sim, C. Choi, S.H. Kim, K.M. Kim, C.J. Lee, Y.T. Kim, X. Lepro, R. H. Baughman, S.J. Kim, Stretchable triboelectric fiber for self-powered kinematic sensing textile, *Sci. Rep.* 6 (2016) 35153.
- [44] K. Dong, Y.C. Wang, J. Deng, Y. Dai, S.L. Zhang, H. Zou, B. Gu, B. Sun, Z.L. Wang, A highly stretchable and washable all-yarn-based self-charging knitting power textile composed of fiber triboelectric nanogenerators and supercapacitors, *ACS Nano* 11 (9) (2017) 9490–9499.
- [45] Z. Zhao, C. Yan, Z. Liu, X. Fu, L.M. Peng, Y. Hu, Z. Zheng, Machine-washable textile triboelectric nanogenerators for effective human respiratory monitoring through loom weaving of metallic yarns, *Adv. Mater.* 28 (46) (2016) 10267–10274.
- [46] K. Dong, J. Deng, W. Ding, A.C. Wang, P. Wang, C. Cheng, Y.-C. Wang, L. Jin, B. Gu, B. Sun, Z.L. Wang, Versatile core-sheath yarn for sustainable biomechanical energy harvesting and real-time human-interactive sensing, *Adv. Energy Mater.* 8 (23) (2018) 1801114.
- [47] L. Jin, S.L. Zhang, S. Xu, H. Guo, W. Yang, Z.L. Wang, Free-fixed rotational triboelectric nanogenerator for self-powered real-time wheel monitoring, *Adv. Mater. Technol.* 6 (3) (2021) 2000918.
- [48] J.K. Tong, X. Huang, S.V. Boriskina, J. Loomis, Y. Xu, G. Chen, Infrared-transparent visible-opaque fabrics for wearable personal thermal management, *ACS Photon.* 2 (6) (2015) 769–778.